# Sodium inversion recovery MRI on the knee joint at 7 T with an optimal control pulse
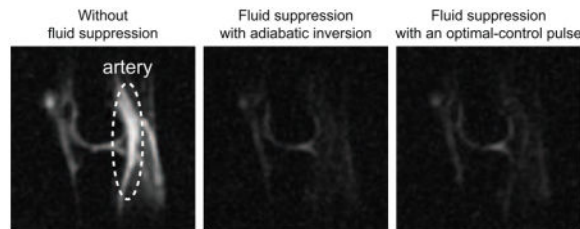
**Jae-Seung Lee**, **Ding Xia**, **Guillaume Madelin**, and **Ravinder R. Regatte**

Department of Radiology, New York University Langone Medical Center, New York, NY 10016, United States

## Abstract

In the field of sodium magnetic resonance imaging (MRI), inversion recovery (IR) is a convenient and popular method to select sodium in different environments. For the knee joint, IR has been used to suppress the signal from synovial fluids, which improves the correlation between the sodium signal and the concentration of glycosaminoglycans (GAGs) in cartilage tissues. For the better inversion of the magnetization vector under the spatial variations of the $B_0$ and $B_1$ fields, the IR sequence usually employ adiabatic pulses as the inversion pulse. On the other hand, it has been shown that RF shapes robust against the variations of the $B_0$ and $B_1$ fields can be generated by numerical optimization based on optimal control theory. In this work, we compare the performance of fluid-suppressed sodium MRI on the knee joint *in vivo*, between one implemented with an adiabatic pulse in the IR sequence and the other with the adiabatic pulse replaced by an optimal-control shaped pulse. While the optimal-control pulse reduces the RF power deposited to the body by 58%, the quality of fluid suppression and the signal level of sodium within cartilage are similar between two implementations.

## Graphical Abstract



## Keywords

Sodium; Knee; MRI; Optimal control; Fermat looped; orthogonally encoded trajectories

---

Corresponding Author: Jae-Seung Lee, Department of Radiology, New York University Langone Medical Center, New York, NY 10016, United States, JaeSeung.Lee@nyumc.org.

## 1. Introduction

In the human body, sodium is an important inorganic nutrient participating in the functioning of nerves and the maintenance of the osmotic balance between cells and surrounding body fluids [1]. The stable isotope $^{23}$Na of sodium, with 100% natural abundance, is a quadrupolar nucleus with a nuclear spin 3/2 and may manifest distinct NMR spectra, depending on its environments in tissues and organs [2]. With the advancement of $^{23}$Na NMR techniques separating different environments and $^{23}$Na MRI methodologies overcoming the low sensitivity due to its lower gyromagnetic ratio and the fast relaxation ascribed to its quadrupolar interactions, $^{23}$Na MRI has been successfully applied for assessing a number of diseases and therapies *in vivo* [3,4].

It has been shown that $^{23}$Na MRI can be useful for the diagnosis of diseases like osteoarthritis and degenerative disc diseases [5,6], in which cartilage tissue is irreversibly degraded. A decrease in the concentration of glycosaminoglycans (GAGs) in cartilage tissue generally indicates the onset of disorder, and the negative charge of GAGs attracts sodium cations into the extracellular matrix of cartilage tissue [7]. Therefore, the concentration of sodium in cartilage tissue is highly correlated with that of GAGs [8–10] so can be considered as a biomarker for the above-mentioned diseases.

Among several methods to generate a contrast between sodium in different tissue environments, fluid suppression through inversion recovery (IR) [11–13] has been one popular sequence for *in vivo* $^{23}$Na MRI [4]. It has been shown that the performance of the fluid-suppressed $^{23}$Na MRI on the knee joint can be improved by employing adiabatic pulses, such as the wide-band uniform rate and smooth truncation (WURST) pulse [14], as the inversion pulse of the IR sequence [13]. Adiabatic pulses help achieve more uniform fluid suppression under the spatial variations of the $B_0$ and $B_1$ fields. In practice, however, their performance is limited due to the finite pulse duration and the restriction on the specific absorption rate (SAR). For example, the inversion of spins may be uneven along the variation of the $B_0$ field if the adiabatic pulse is implemented through the linear sweeping of frequency offsets and its duration is comparable to the relaxation times.

The performance of inversion under fast relaxation may be improved by employing a certain shaped RF pulse in place of adiabatic pulses. Optimal control theory [15,16] provides a convenient and flexible algorithm to find a shaped RF pulse for targeted performance [17–23], and its application to $^{23}$Na NMR and MRI has been successful [24–26]. Here, we present an optimal-control (OC) pulse for fluid-suppressed $^{23}$Na MRI on the knee joint *in vivo* and compare its performance with the WURST pulse numerically and experimentally. We will also discuss how the choice of a cost function and the range of the $B_1$ field included for numerical optimization affect the performance of resulting OC pulses.

## 2. Methods

### 2.1. Numerical optimization

An OC pulse was searched in order to maximize a cost function

$$\phi = (+\hat{e}_3) \cdot \mu_1(t_p) + (-\hat{e}_3) \cdot \mu_2(t_p), \quad (1)$$

where $\hat{e}_3$ is the unit vector along the $z$ direction, $t_p$ is the duration of an OC pulse, and $\mu_{1,2}(t_p)$ are respectively the final states of the magnetization vectors of systems 1 and 2. The detailed OC algorithm used in this work is presented in Appendix A. Assuming that the spin-spin relaxation time ($T_2$) is same as the spin-lattice relaxation time ($T_1$), the relaxation times of the systems 1 and 2 were set to be 20 ms and 38 ms, respectively, which are close to the $T_1$ relaxation times of $^{23}$Na in cartilage and blood *in vivo* at 7 T [27]. The pulse duration $t_p$ was 10 ms, and the maximum RF amplitude ($\omega_{1,max}/2\pi$) was set to be 250 Hz, which was implemented by adding a large value to the cost function when $|\omega_1| > \omega_{1,max}$. The numerical optimization was performed over the frequency offsets from –160 Hz to 160 Hz with a step size of 4 Hz and the scale of the RF amplitude or the RF scale factors from 0.6 to 1.2 with a step size of 0.05.

## 2.2. In vivo $^{23}$Na knee MRI

After approval from the Institutional Review Board of the New York University Langone Medical Center and signed informed consent, the right knee joints of five healthy volunteers (3 males (mean age = 38.3 ± 7.6 years) and 2 females (mean age = 31.0 ± 4.2 years); mean age = 35.6 ± 7.1 years) was scanned on a 7 T Siemens scanner with an in-house built double-tuned coil with eight $^{23}$Na channels and four $^1$H channels [28]. For each volunteer, three knee images were acquired by $^{23}$Na MRI, one without fluid suppression and the other two with fluid suppression, performed with the WURST and OC pulses.

The knee images were acquired with Fermat looped, orthogonally encoded trajectories (FLORET [29]) consisting of 3 hubs at 45°, each of which comprises 332 interleaves. The parameters for the image acquisition were field of view (FOV) = (220 mm)$^3$, echo time (TE) = 0.2 ms, repetition time (TR) = 140 ms, Nyquist resolution = 3.4 mm, the acquisition time = 6.6 ms, 6 averages, the duration of the excitation pulse = 0.6 ms, and the total acquisition time = ~14 mins. With fluid suppression, an inversion pulse and a recovery delay (TI) preceded the excitation pulse. In this work, TI was defined as the time interval from the end of the inversion pulse to the beginning of the excitation pulse. The TIs were 19 ms and 16 ms for the WURST and OC pulses, respectively. The schematic of the pulse sequence is shown in Fig. 1(a).

The spatial variation of the $B_1$ field in the knee joint was estimated by the double angle method [30]. An additional image was acquired with the excitation pulse at the flip angle of $\pi/4$, and the signal intensities were compared with those acquired with the excitation pulse at the flip angle of $\pi/2$. So the flip angle was estimated by $\cos^{-1}[I_{\pi/4}/(2I_{\pi/2})]$ in radians, where $I_\theta$ indicates the signal intensity measured with the excitation pulse at the flip angle $\theta$. Since $\theta = \gamma B_1 t_p$, we defined $\cos^{-1}[I_{\pi/4}/(2I_{\pi/2})]/(\pi/4)$ as a $B_1$ scale factor.

## 2.3. Data processing

Standard 3D regridding [31] was used to reconstruct the images with the nominal resolution of 2 mm. For each volunteer, six regions of interest (ROIs) were defined on artery, patella

cartilage, lateral and medial femorotibial cartilage, and lateral and medial femoral condyle cartilage.

After normalized to the signal intensities measured without fluid suppression, paired samples $t$-tests were performed on the signal intensities from the fluid-suppressed $^{23}$Na knee images obtained with the WURST and OC pulses.

## 3. Results and discussion

### 3.1. Simulated performance of an OC pulse

The RF waveforms of the WURST and OC pulses used in this work are presented in Figs. 1(b) and 1(c). The RF amplitude and phase of the WURST pulse are respectively described as

$$\omega_1(1-|\sin\beta(t)|^{20}) \quad (2)$$

and

$$\pi f_{max} (2t-t_p)^2/(2t_p) \quad (3)$$

with $t_p = 10$ ms, $0 \quad t \quad t_p$, $\omega_1/2\pi = 250$ Hz, $\beta(t) = (\pi/2) (2t-t_p)/t_p$, and $f_{max} = 1$ kHz. The phase change for $0 \quad t \quad t_p$ produces a linear frequency sweep ranging from $-f_{max}$ to $+f_{max}$. The y component of the OC pulse was zero by design. The root-mean-square (r.m.s.) RF amplitudes of the WURST and OC pulses are respectively 19.5 µT and 9.9 µT, so the OC pulse requires only 25.8% of the RF power carried by the WURST pulse.

The z components of the magnetization vectors at the end of the WURST and OC pulses, i.e., $\hat{e}_3 - \mu_k(t_p)$ where $k = 1$ and 2, were obtained by numerically solving the Bloch equations with the initial thermal equilibrium state, i.e. $\mu_k(0) = \hat{e}_3$, and are presented in Fig. 2 as contour plots against the frequency offsets and the RF scale factors. As shown in Figs. 2(b) and 2(c), the relatively long duration of the WURST pulse may cause the uneven inversion of the spins along the frequency offsets because the spins inverted at the earlier moments have more time to relax toward the thermal equilibrium state than those inverted at the later moments. The performance of the WURST pulse degrades as the RF amplitude decreases, probably because the adiabatic condition is not satisfied at such low RF amplitudes [13].

As for the OC pulse, its performance along the frequency offsets is symmetric with respect to the zero frequency offset, as shown in Figs. 2(f) and 2(g). The OC pulse manifests certain robustness against the B$_1$ variation if the RF scale factor is between 0.8 and 1.2, although the performance degrades when the RF amplitude is reduced by more than 20%.

While the OC pulse inverts the spins of the individual systems less efficiently than the WURST pulse, it may separate the two systems from each other more effectively, as seen in Figs. 2(d) and 2(h) where the difference between $\hat{e}_3 \cdot \mu_1(t_p)$ and $\hat{e}_3 \cdot \mu_2(t_p)$ are presented. In addition, the level of the difference seems more uniform against the frequency offsets and

the RF scale factors. Notice that the OC pulse resulted from maximizing the difference between $\hat{e}_3 \cdot \mu_1(t_p)$ and $\hat{e}_3 \cdot \mu_2(t_p)$ under the variation of the $B_0$ and $B_1$ fields.

## 3.2. In vivo $^{23}$Na knee MRI

As an example, representative slices from $^{23}$Na 3D images of the right knee of a healthy volunteer are presented in Fig. 3. Without fluid suppression, the $^{23}$Na image clearly displays the artery, as indicated in Fig. 3(a). With fluid suppression, TI's were chosen to suppress the artery, as seen in Figs. 3(b) and 3(c). While the value of TI for the WURST pulse was taken from the previous work [13, 32, 33], the TI for the OC pulse was chosen based on the inversion profile shown in Fig. 2(f) and the corresponding relaxation time (= 38 ms).

In order to compare the performances of the two fluid-suppressed $^{23}$Na MRI's, the box plots of the signal intensities, after normalized to ones acquired without fluid suppression, are presented in Fig. 4 for individual ROIs and subjects. As for the suppression of arteries, the signal intensities from the arteries acquired with the OC pulse were lower for two subjects or higher for two subjects than those acquired with the WURST pulse. For one remaining case, the difference between the signal intensities from the two fluid-suppressed $^{23}$Na MRI's was not statistically significant (Subject #5 in Fig. 4(a)). In terms of fluid suppression, therefore, the performances of the two sequences may be considered similar.

This fluctuation in fluid suppression seems related to the variation of the RF scale factor. The standard deviations of the $B_1$ scale factors for the individual subjects, as shown in Table 1, were estimated smaller in the arteries when the fluid suppression was better with the OC pulse, and vice versa. As shown in Figs. 2(c) and 2(g), the performance of the OC pulse is more sensitive than the WURST pulse, to the variation of the RF scale factor when it is between 0.6 and 0.8. Since the mean values of the $B_1$ scale factors in the arteries were above 0.8, as shown in Table 1, how low the $B_1$ field was in the arteries, which is reflected in the standard deviations, probably resulted in the varying performances on the suppression of arteries between the OC and WURST pulses.

For cartilage tissues, the images acquired with the OC pulse produced higher signal intensities for the most cases. There were four instances in which the differences between the signal intensities from the two fluid-suppressed $^{23}$Na MRI's were not statistically significant (lateral femoral condyle for Subjects #2 and #4, patella for Subject #3, and medial femoral condyle for Subject #4). As shown in Figs. 2(b) and 2(f), the z component of the magnetization vector for the system with $T_1$ = 20 ms is less inverted with the OC pulse [$\hat{e}_3 \cdot \mu_1(t_p)$ = −0.42 ± 0.16 within the red box in Fig. 2(f)] than with the WURST pulse [$\hat{e}_3 \cdot \mu_1(t_p)$ = −0.56 ± 0.17 within the red box in Fig. 2(b)]. After TI's, however, the z components of the magnetization vector may end up at the almost same value (0.465 ± 0.058 for the WURST pulse vs. 0.468 ± 0.061 for the OC pulse), because of the longer TI with the WURST pulse.

Note that $^{23}$Na in cartilage tissues may experience quadrupolar couplings and bi-exponential relaxation, which causes $T_2^*$ to be much shorter than $T_1$ [2–4]. While the inversion may not be as efficient as simulated for $^{23}$Na in cartilage tissues, it would not be important in terms of fluid suppression. In order to properly simulate the dynamics, on the other hand, the

quantum master equations should be solved with the knowledge of quadrupolar coupling constants and quadrupolar relaxation times. It would not be so difficult to incorporate the quantum master equations into the OC algorithm [24–26], although the quarupolar couplings of $^{23}$Na in cartilage tissues *in vivo* are currently unavailable. Based on the relaxation times reported in Ref. [27], a numerical simulation including the bi-exponential relaxation of $^{23}$Na showed that the z component of the magnetization vector may reach a higher value with the WURST pulse ($0.59 \pm 0.03$ for the WURST pulse vs. $0.58 \pm 0.05$ for the OC pulse). Note that these estimations took all the frequency offsets and rf scale factors equally, without considering their actual distributions *in vivo*.

While the performance of fluid-suppressed $^{23}$Na knee MRI would not change much when the OC pulse is used in place of the WURST pulse, with TI accordingly adjusted, the SAR may be reduced since the OC pulse requires less RF power than the WURST pulse (See *Section 3.1*). The SAR values displayed on the MRI scanner were 15% for the FLORET sequence without fluid suppression, and 78–80% and 33% for the fluid-suppressed MRI's with the WURST and OC pulses, respectively. The reduction of the displayed SAR value by about 58% from the one with the WURST pulse to the other with the OC pulse is consistent with the difference between their numerical r.m.s. RF amplitudes presented in *Section 3.1*.

### 3.3. $B_1$-field inhomogeneity

Since the gyromagnetic ratio of $^{23}$Na is only 26% of the proton's, the spatial inhomogeneity of the $B_0$ field may not be a major concern for the numerical optimization. The range of the frequency offsets used in the numerical optimization, which spans about 4 ppm for $^{23}$Na at 7 T, seemed enough to cover the spatial variation of the $B_0$ field in the knee joint, although the resonance offsets inside some gel phantoms might be out of the range, as seen in Fig. 3(c). In order to determine the range of the RF scale factors, on the other hand, we measured a $B_1$-field map and compared the performances of OC pulses optimized with the varying ranges of the RF scale factors.

For one healthy volunteer, the box plots of the $B_1$ scale factors in the individual ROIs defined on a $^{23}$Na knee image are presented in Fig. 5. On the same subject, we investigated the performances of three OC pulses, which were optimized under different ranges of the RF scale factors. While keeping the upper limit of the RF scale factor at 1.2, the lower limit was varied from 0.6 to 0.8. Box plots of the signal intensities acquired with these OC pulses are presented in Fig. 6 for the individual ROIs, along with those acquired with the WURST pulse and without fluid suppression.

Extending the range of the RF scale factors helped improve the suppression of the signal from artery, as seen in Fig. 6(a), while the signal intensities from cartilage tissues were kept similar between the three OC pulses, as shown in Figs. 6(b)–6(f). We have performed one-way analysis of variance (ANOVA) on the distributions of the signal intensities acquired with the three OC pulses and indicated the p values in Fig. 6, which support the above-mentioned observations.

### 3.4. Choice of a cost function

When IR is used to separate two systems with different relaxation times, TI is usually determined by the parameters of the system to be suppressed, which is given as

$$T_1 \ln[1 - M_z(t=0)/M_0] \quad (4)$$

with $T_1$, $M_z(t=0)$, and $M_0$, respectively being the spin-lattice relaxation time, the z component of the magnetization vector after the inversion pulse, and the z component of the magnetization vector at the thermal equilibrium state, of the system to be suppressed. Indeed, our first cost function was

$$\phi' = (-\hat{e}_3) \cdot \mu_2(t_p), \quad (5)$$

which takes into account only the system to be suppressed. Interestingly, the two cost functions $\varphi$ and $\phi'$ produced distinct RF waveforms. As an example, Fig. 7(a) displays the OC pulses maximizing $\varphi$ and $\phi'$, optimized over the frequency offsets from −160 Hz to 160 Hz with a step size of 4 Hz and the RF scale factors from 0.8 to 1.2 with a step size of 0.05. When they were tested *in vivo*, the shape maximizing $\varphi$ resulted in better fluid suppression, which does not imply that $\varphi$ would always be a better choice than $\phi'$. Notice that we did not try $\phi'$ for the larger ranges of the RF scale factors.

For these two OC pulses and the WURST pulse, the evolutions of the z components of the magnetization vectors for the systems with $T_1 = 20$ ms and 38 ms were evaluated at the frequency offset of 0 Hz and ±100 Hz and the RF scale factor of 1.0, which are presented in Figs. 7(b) and 7(c). The WURST pulse is supposed to flip a spin when its frequency sweep crosses the resonance frequency of the spin. As seen in Figs. 7(b) and 7(c), the z components of the magnetization vectors display huge changes when the WURST pulse passes the corresponding frequency offsets, are almost inverted, and relax back toward the thermal equilibrium state in accordance with the corresponding relaxation times. For the OC pulse maximizing the cost function $\phi'$, the evolutions of the magnetization vectors show that the inversions may happen at the end of the pulse [34], which might not give enough time for the two systems to be separated according to the relaxation times during the remaining pulse duration. In other words, the OC pulse maximizing the cost function $\phi'$ seems more robust against the variation of the relaxation time than the WURST pulse, although the optimization was performed with a single relaxation time. By contrast, the OC pulse maximizing the cost function $\varphi$ inverts the magnetization vectors at the beginning so that it allows more time for the relaxation. At the end of the pulse duration, it produces larger difference between the z components of the two magnetization vectors than the WURST pulse, as shown in Figs. 7(b) and 7(c).

Comparing with the conventional selective inversion pulses such as the minimum-phase Shinnar-Le Roux (SLR) inversion pulse [35] and spin-inversion band-selective, uniform response, pure-phase pulse (I-BURP) [36], the OC pulses are not so oscillatory and their RF amplitudes do not get weakened even while any noticeable inversion is happening. In this

work, the OC pulses were not band-selective and their RF amplitudes were restricted by design, so the more or less uniform performance under the variations of the $B_0$ and $B_1$ fields could be achieved without excessive amplitude modulation.

## 4. Summary

Fluid-suppressed $^{23}$Na MRI on the knee joint *in vivo* has been implemented with an OC pulse in place of the inversion pulse in the IR sequence for fluid suppression. The scans on the knee joints of five healthy volunteers at 7 T demonstrated that two fluid-suppressed $^{23}$Na MRI's performed with the OC and WURST pulses were similar regarding their performances of fluid suppression and contrast for cartilage tissues. One practically important benefit of using the OC pulse developed in this study is the reduction of the SAR, which may be exploited to improve the performance of the image acquisition in terms of the scan time and/or the signal-to-noise ratio.

The performance of fluid-suppressed $^{23}$Na MRI may be further improved if the excitation pulse is made more robust against the variations of the $B_0$ and $B_1$ fields, which can also be realized by designing an OC pulse for the signal excitation. In the end, a single OC pulse may implement the entire fluid-suppressed $^{23}$Na MRI, which would require better knowledge about the quadrupolar coupling constants and relaxation times of $^{23}$Na in the knee joint *in vivo*. In any case, we expect OC pulses to lighten some practical limitations of $^{23}$Na MRI and to contribute to extending its use as a diagnostic tool.

## Acknowledgments

## References

1. Reece, JB.; Urry, LA.; Cain, ML.; Wasserman, SA.; Minorsky, PV.; Jackson, RB. Campbell Biology. 9. Benjamin Cummings; San Francisco: 2011.

2. Rooney WD, Springer CS. A comprehensive approach to the analysis and interpretation of the resonances of spins 3/2 from living systems. NMR Biomed. 1991; 4:209–226.10.1002/nbm.1940040502 [PubMed: 1751345]

3. Madelin G, Regatte RR. Biomedical applications of sodium MRI in vivo. J Magn Reson Imaging. 2013; 38:511–29.10.1002/jmri.24168 [PubMed: 23722972]

4. Madelin G, Lee JS, Regatte RR, Jerschow A. Sodium MRI: methods and applications. Prog Nucl Magn Reson Spectrosc. 2014; 79:14–47.10.1016/j.pnmrs.2014.02.001 [PubMed: 24815363]

5. Gold GE, Burstein D, Dardzinski B, Lang P, Boada F, Mosher T. MRI of articular cartilage in OA: novel pulse sequences and compositional/functional markers. Osteoarthr Cartil. 2006; 14:A76–A86.10.1016/j.joca.2006.03.010 [PubMed: 16716605]

6. Insko EK, Clayton DB, Elliott MA. In Vivo Sodium MR Imaging of the Intervertebral Disk at 4 T. Acad Radiol. 2002; 9:800–4.10.1016/s1076-6332(03)80350-1 [PubMed: 12139094]

7. Hu, JCY.; Athanasiou, KA. Structure and Function of Articular Cartilage. In: An, YH.; Martin, KL., editors. Handbook of Histology Methods for Bone and Cartilage. Humana Press; Totowa: 2003. p. 73-95.

8. Navon G, Shinar H, Eliav U, Seo Y. Multiquantum filters and order in tissues. NMR Biomed. 2001; 14:112–32.10.1002/nbm.687 [PubMed: 11320537]

9. Rong P, Regatte RR, Jerschow A. Clean demarcation of cartilage tissue $^{23}$Na by inversion recovery. J Magn Reson. 2008; 193:207–9.10.1016/j.jmr.2008.04.036 [PubMed: 18502158]

10. Choy J, Ling W, Jerschow A. Selective detection of ordered sodium signals via the central transition. J Magn Reson. 2006; 180:105–9.10.1016/j.jmr.2006.01.011 [PubMed: 16469514]

11. Kline RP, Wu EX, Petrylak DP, Szabolcs M, Alderson PO, Weisfeldt ML, Cannon P, Katz J. Rapid in vivo monitoring of chemotherapeutic response using weighted sodium magnetic resonance imaging. Clin Cancer Res. 2000; 6:2146–56. [PubMed: 10873063]

12. Stobbe R, Beaulieu C. In vivo sodium magnetic resonance imaging of the human brain using soft inversion recovery fluid attenuation. Magn Reson Med. 2005; 54:1305–10.10.1002/mrm.20696 [PubMed: 16217782]

13. Madelin G, Lee JS, Inati S, Jerschow A, Regatte RR. Sodium inversion recovery MRI of the knee joint in vivo at 7T. J Magn Reson. 2010; 207:42–52.10.1016/j.jmr.2010.08.003 [PubMed: 20813569]

14. Kupce E, Freeman R. Adiabatic Pulses for Wideband Inversion and Broadband Decoupling. J Magn Reson A. 1995; 115:273–6.10.1006/jmra.1995.1179

15. Kirk, DE. Optimal Control Theory: An Introduction. Prentice-Hall, Inc; Englewood Cliffs: 1970.

16. Bertsekas, DP. Dynamic Programming and Optimal Control. 3. Vol. 1. Athena Scientific; Nashua: 2005.

17. Conolly S, Nishimura D, Macovski A. Optimal control solutions to the magnetic resonance selective excitation problem. IEEE Trans Med Imaging. 1986; 5:106–15.10.1109/TMI. 1986.4307754 [PubMed: 18243994]

18. Rosenfeld D, Zur Y. Design of adiabatic selective pulses using optimal control theory. Magn Reson Med. 1996; 36:401–9.10.1002/mrm.1910360311 [PubMed: 8875410]

19. Mao J, Mareci TH, Scott KN, Andrew ER. Selective inversion radiofrequency pulses by optimal control. J Magn Reson. 1986; 70:310–8.10.1016/0022-2364(86)90016-8

20. Skinner TE, Reiss TO, Luy B, Khaneja N, Glaser SJ. Application of optimal control theory to the design of broadband excitation pulses for high-resolution NMR. J Magn Reson. 2003; 163:8–15.10.1016/S1090-7807(03)00153-8 [PubMed: 12852902]

21. Khaneja N, Reiss T, Kehlet C, Schulte-Herbrüggen T, Glaser SJ. Optimal control of coupled spin dynamics: design of NMR pulse sequences by gradient ascent algorithms. J Magn Reson. 2005; 172:296–305.10.1016/j.jmr.2004.11.004 [PubMed: 15649756]

22. Gershenzon NI, Kobzar K, Luy B, Glaser SJ, Skinner TE. Optimal control design of excitation pulses that accommodate relaxation. J Magn Reson. 2007; 188:330–6.10.1016/j.jmr.2007.08.007 [PubMed: 17804269]

23. Lapert M, Zhang Y, Janich MA, Glaser SJ, Sugny D. Exploring the Physical Limits of Saturation Contrast in Magnetic Resonance Imaging. Sci Rep. 2012; 2:589.10.1038/srep00589

24. Lee JS, Regatte RR, Jerschow A. Optimal nuclear magnetic resonance excitation schemes for the central transition of a spin 3/2 in the presence of residual quadrupolar coupling. J Chem Phys. 2008; 129:224510.10.1063/1.3036005 [PubMed: 19071931]

25. Lee JS, Regatte RR, Jerschow A. Optimal excitation of $^{23}$Na nuclear spins in the presence of residual quadrupolar coupling and quadrupolar relaxation. J Chem Phys. 2009; 131:174501.10.1063/1.3253970 [PubMed: 19895019]

26. Lee JS, Regatte RR, Jerschow A. Optimal control NMR differentiation between fast and slow sodium. Chem Phys Lett. 2010; 494:331–6.10.1016/j.cplett.2010.06.019

27. Madelin G, Jerschow A, Regatte RR. Sodium relaxation times in the knee joint in vivo at 7T. NMR Biomed. 2011; 25:530–7.10.1002/nbm.1768 [PubMed: 21853493]

28. Brown R, Madelin G, Lattanzi R, Chang G, Regatte RR, Sodickson DK, Wiggins GC. Design of a nested eight-channel sodium and four-channel proton coil for 7T knee imaging. Magn Reson Med. 2013; 70:259–68.10.1002/mrm.24432 [PubMed: 22887123]

29. Pipe JG, Zwart NR, Aboussouan EA, Robison RK, Devaraj A, Johnson KO. A new design and rationale for 3D orthogonally oversampled k-space trajectories. Magn Reson Med. 2011; 66:1303–11.10.1002/mrm.22918 [PubMed: 21469190]

30. Stollberger R, Wach P. Imaging of the active $B_1$ field in vivo. Magn Reson Med. 1996; 35:246–51.10.1002/mrm.1910350217 [PubMed: 8622590]

31. Pipe JG, Menon P. Sampling density compensation in MRI: Rationale and an iterative numerical solution. Magn Reson Med. 1999; 41:179–86.10.1002/(SICI)1522-2594(199901)41:1<179::AID-MRM25>3.0.CO;2-V [PubMed: 10025627]

32. Madelin G, Babb JS, Xia D, Chang G, Jerschow A, Regatte RR. Reproducibility and repeatability of quantitative sodium magnetic resonance imaging in vivo in articular cartilage at 3 T and 7 T. Magn Reson Med. 2012; 68:841–9.10.1002/mrm.23307 [PubMed: 22180051]

33. Madelin G, Babb J, Xia D, Chang G, Krasnokutsky S, Abramson SB, Jerschow A, Regatte RR. Articular cartilage: evaluation with fluid-suppressed 7.0-T sodium MR imaging in subjects with and subjects without osteoarthritis. Radiology. 2013; 268:481–91.10.1148/radiol.13121511 [PubMed: 23468572]

34. Gershenzon NI, Kobzar K, Luy B, Glaser SJ, Skinner TE. Optimal control design of excitation pulses that accommodate relaxation. J Magn Reson. 2007; 188:330–6.10.1016/j.jmr.2007.08.007 [PubMed: 17804269]

35. Pauly J, Le Roux P, Nishimura D, Macovski A. Parameter relations for the Shinnar-Le Roux selective excitation pulse design algorithm. IEEE Trans Med Imaging. 1991; 10:53–65.10.1109/42.75611 [PubMed: 18222800]

36. Geen H, Freeman R. Band-selective radiofrequency pulses. 1991; 93:93–141.10.1016/0022-2364(91)90034-q

37. Levante TO, Ernst RR. Homogeneous Versus Inhomogeneous Quantum-Mechanical Master-Equations. Chem Phys Lett. 1995; 241:73–8.10.1016/0009-2614(95)00578-R

38. Helgstrand M, Härd T, Allard P. Simulations of NMR pulse sequences during equilibrium and non-equilibrium chemical exchange. J Biomol NMR. 2000; 18:49–63.10.1023/A:1008309220156 [PubMed: 11061228]

39. Press, WH.; Teukolsky, SA.; Vetterling, WT.; Flannery, BP. Numerical Recipes in C. 2. Cambridge University Press; New York: 1992.

## Appendix

## A. Optimal-control algorithm for RF pulse design

Here, we present the algorithm for finding RF shaped pulses based on optimal control theory [25,26]. First, we assume that the time evolution of a given system can be modeled by a set of first-order differential equations:

$$\frac{d}{dt}\mu(t) = -P(t)\mu(t), \quad \text{(A1)}$$

where $\mu(t)$ and $P(t)$ respectively represent the state of a system and the transition matrix at $t$. For a spin-1/2, the Bloch equations with the $T_1$ and $T_2$ relaxation terms can be easily converted to the homogeneous form like Eq. (A1) [37,38]. We also assume that the transition matrix $P(t)$ can be expressed as $P(t) = P_0 + \Sigma_k P_k u_k(t)$, where $P_0$ is the time-independent part and each $P_k$ corresponds to the control parameter $u_k(t)$.

For an RF shape consisting of $N$ even time steps, there are $2N$ control parameters, $N$ parameters for the x component of the RF amplitude $\omega_{1x}$ and the other $N$ for the y component $\omega_{1y}$. Defining $\Delta t$ as $t_p/N$, where $t_p$ is the duration of the RF shaped pulse,

$$u_k(t) = \begin{cases} \omega_{1x}(k), & 1 \le k \le N \\ \omega_{1y}(k-N), & N+1 \le k \le 2N \end{cases}$$ for $(k-1)\Delta t \le t < k\Delta t$, and 0 otherwise. Therefore,

$$P(t) = \begin{bmatrix} 0 & 0 & 0 & 0 \\ 0 & \frac{1}{T_2} & \Delta\omega_0 & -\omega_{1y}(k-N) \\ 0 & -\Delta\omega_0 & \frac{1}{T_2} & \omega_{1x}(k) \\ -\frac{2}{T_1} & \omega_{1y}(k-N) & -\omega_{1x}(k) & \frac{1}{T_1} \end{bmatrix} \quad \text{(A2)}$$

for $(k-1)\,\tau t \leq t < k\,\tau t$, where $\Delta\omega_0$ is the resonance offset, such that

$$P_0 = \begin{bmatrix} 0 & 0 & 0 & 0 \\ 0 & \frac{1}{T_2} & \Delta\omega_0 & 0 \\ 0 & -\Delta\omega_0 & \frac{1}{T_2} & 0 \\ -\frac{2}{T_1} & 0 & 0 & \frac{1}{T_1} \end{bmatrix} \quad \text{(A3)}$$

and

$$P_k = \begin{cases} \begin{bmatrix} 0 & 0 & 0 & 0 \\ 0 & 0 & 0 & 1 \\ 0 & 0 & 0 & 1 \\ 0 & 0 & -1 & 0 \end{bmatrix}, & 1 \leq k \leq N \\ \begin{bmatrix} 0 & 0 & 0 & 0 \\ 0 & 0 & 0 & -1 \\ 0 & 0 & 0 & 0 \\ 0 & 1 & 0 & 0 \end{bmatrix}, & N+1 \leq k \leq 2N \end{cases} \quad \text{(A4)}$$

Second, given a cost function $\Phi$ to be minimized, the corresponding objective function can be constructed with a help of a vector Lagrange multiplier $\lambda$ as

$$J = \Phi + \int_0^{t_p} \left[ \lambda^\dagger \left( \frac{d\mu}{dt} + P\mu \right) + \left( \frac{d\mu^\dagger}{dt} + P^\dagger \mu^\dagger \right) \lambda \right] dt. \quad \text{(A5)}$$

Here, we include the complex conjugate term in the integral to make $J$ real because the components of $\mu$ and $P$ are in general complex. It is straightforward to show that the variation of $J$ can be made zero when

$$\frac{d}{dr}\lambda^\dagger(t) = \lambda^\dagger(t)P(t), \quad \text{(A6)}$$

$$\lambda^\dagger(t_p) = -\frac{1}{2}\frac{\delta\Phi}{\delta\mu(t_p)}, \quad \text{(A7)}$$

and

$$(\lambda^\dagger P_k \mu + \mu^\dagger P_k \lambda)\delta u_k = 0 \text{ for each } k. \quad \text{(A8)}$$

While Eqs. (A6) and (A7) respectively provide a set of first-order differential equations governing the evolution of $\lambda$ and the initial condition at $t_p$. Eq. (A8) offers the conditions for stationary or 'optimal' trajectories followed by $\mu$ and $\lambda$. It would not be trivial to analytically

solve Eqs. (A1), (A6), and (A8) simultaneously, so one usually relies on numerical iterative approaches in the form of the optimization of $J$. In such approaches, trajectories followed by $\mu$ and $\lambda$ are evaluated by using Eqs. (A1) and (A6) under prescribed $u_k(t)$'s to calculate $\lambda^\dagger P_k \mu + \mu^\dagger P_k \lambda$ for each $k$, which can be seen as $\delta J / \delta u_k$ and constitutes the gradient of $J$. So $u_k(t)$'s may be updated to increase or decrease $J$ and used to repeat the evaluation of new trajectories and gradient. The iteration may stop when the relative change in the value of $J$ does not exceed a certain threshold (for example, $10^{-6}$). In this work, we used the conjugate gradient method according to the Polak-Ribière formula [39].

## Highlights

- Optimal control theory was used to find a shaped pulse for fluid-suppressed $^{23}$Na MRI.

- The performance of the shaped pulse was demonstrated through *in vivo* knee MRI.

- The fluid suppression was as good as the conventional method.

- Higher signal intensities were produced in cartilage tissues.

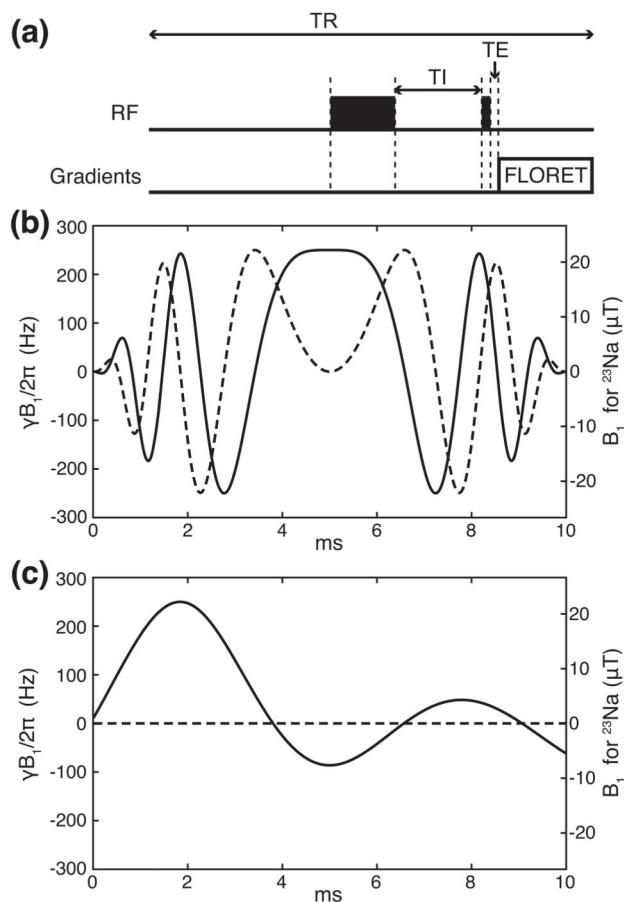- The RF power deposition to the body was reduced by 58%.

**Figure 1.**
RF waveforms used in this study. (a) The schematic of the fluid-suppressed $^{23}$Na MRI pulse sequence during a single TR, with the delays TI and TE indicated. The wide and thin black boxes represent the inversion and excitation pulses, respectively. The signal is acquired in sync with the FLORET sequence. Note that the length along the abscissa is not proportional to real time. (b) WURST, an adiabatic inversion pulse. (c) An OC pulse maximizing the difference in the z component of the magnetization vector between spins with $T_1 = 20$ ms and 38 ms. The solid and dashed lines represent the x and y components of RF waveforms, respectively. The gyromagnetic ratio of $^{23}$Na is 11.262 MHz/T.
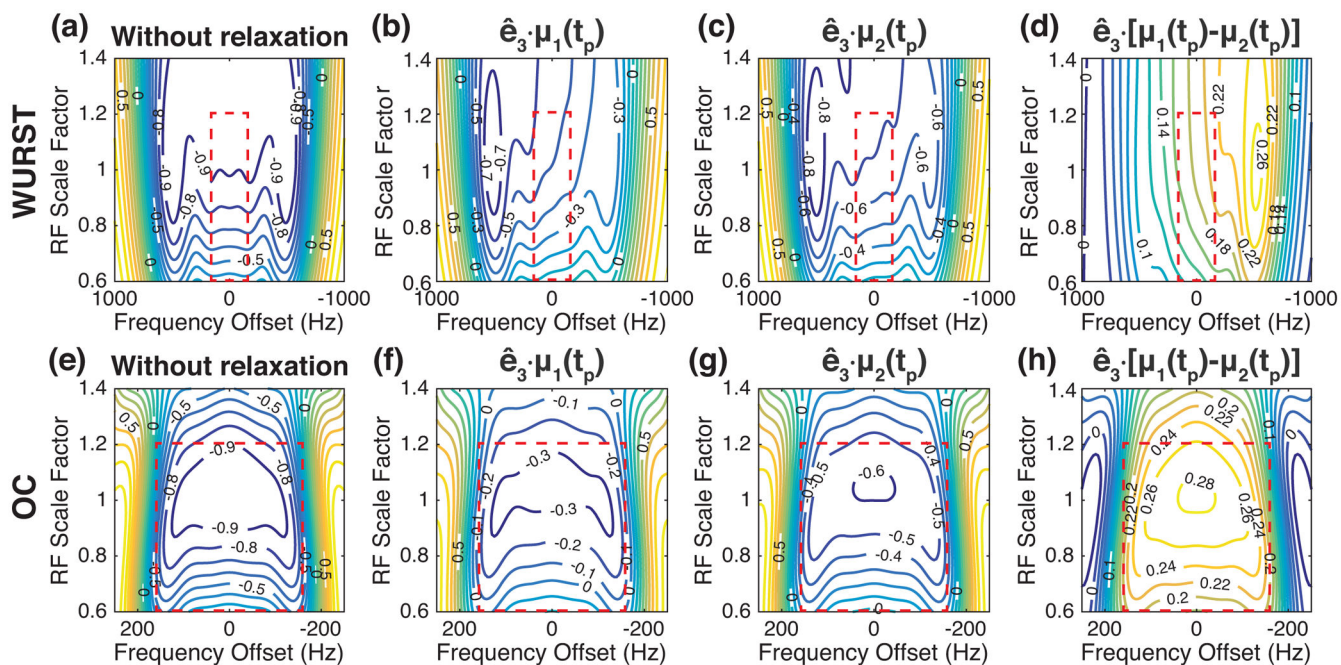
**Figure 2.**
The *z* components of the magnetization vectors as a function of the frequency offset and the RF scale factor, at the end of the WURST and OC pulses applied to the thermal equilibrium state. (a–c) The contour plots of the z components after applying the WURST pulse for the system without relaxation (a) and with $T_1 = T_2 = 20$ ms (b) and 38 ms (c). (d) The difference between the contour plots shown in (b) and (c). (e–g) The contour plots of the z components after applying the OC pulse for the system without relaxation (e) and with $T_1 = T_2 = 20$ ms (f) and 38 ms (g). (h) The difference between the contour plots shown in (f) and (g). The red box indicates the range of the frequency offsets and RF scale factors included in the numerical optimization.
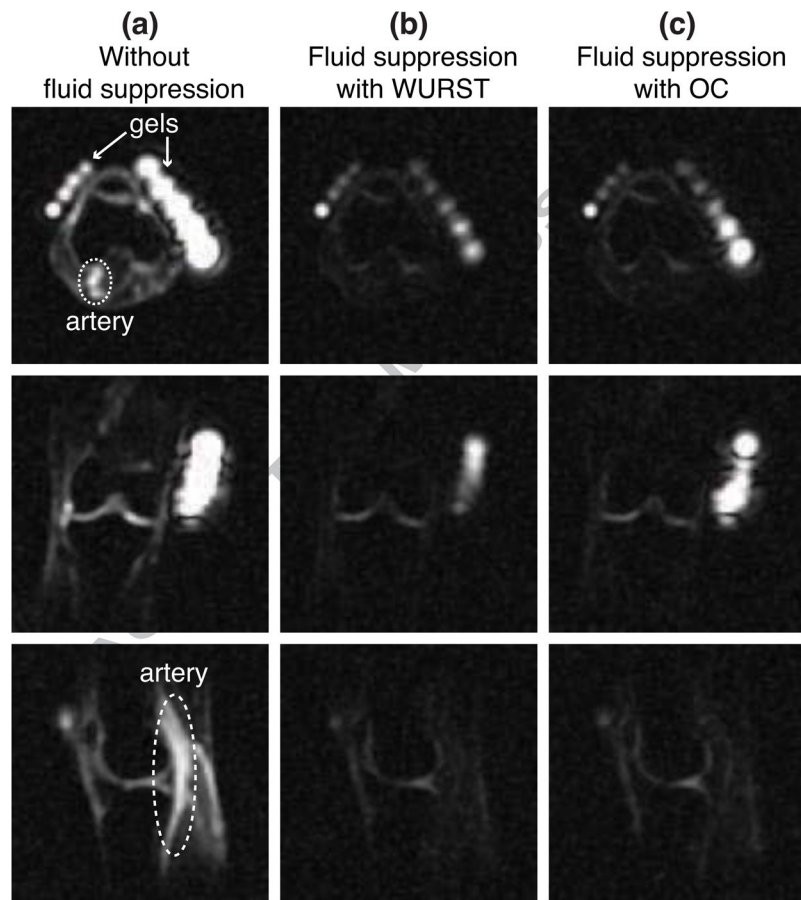
**Figure 3.**
Slices from $^{23}$Na images of the right knee of a healthy volunteer. (a) Slices from the $^{23}$Na image obtained without fluid suppression. The artery and gel phantoms are indicated. (b) Slices from fluid-suppressed $^{23}$Na MRI performed with the WURST pulse and TI = 19 ms. (c) Slices from fluid-suppressed $^{23}$Na MRI performed with the OC pulse and TI = 16 ms.
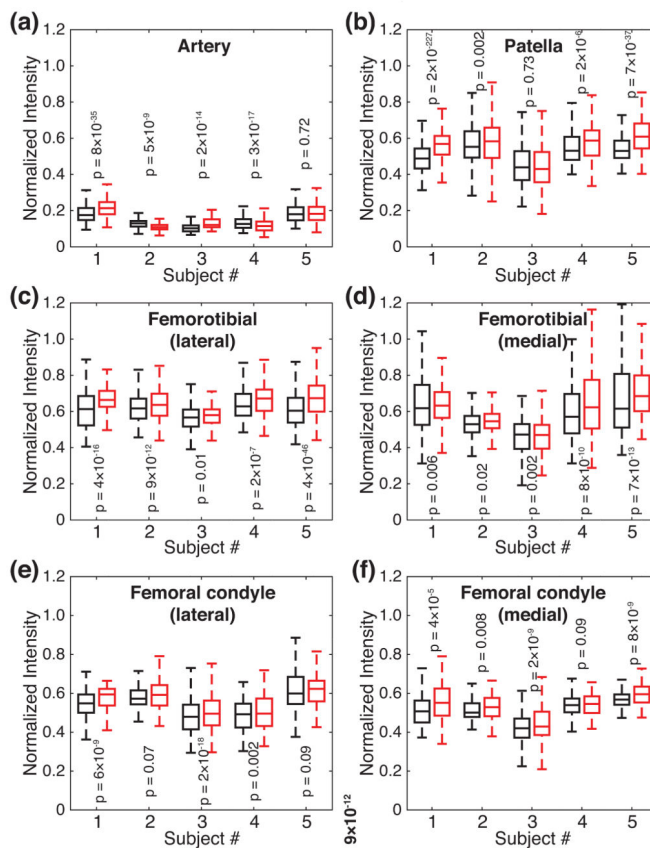
**Figure 4.**
Box plots of the signal intensities from the fluid-suppressed $^{23}$Na MRI's performed with the WURST (black boxes) and OC (red boxes) pulses, after normalized to the signal intensities from $^{23}$Na MRI performed without fluid suppression. (a) Artery. (b) Patellar cartilage. (c) Femorotibial cartilage, lateral. (d) Femorotibial cartilage, medial. (e) Cartilage on femoral condyle, lateral. (f) Cartilage on femoral condyle, medial. For each pair of the distributions, the p value from paired samples *t*-test is displayed.
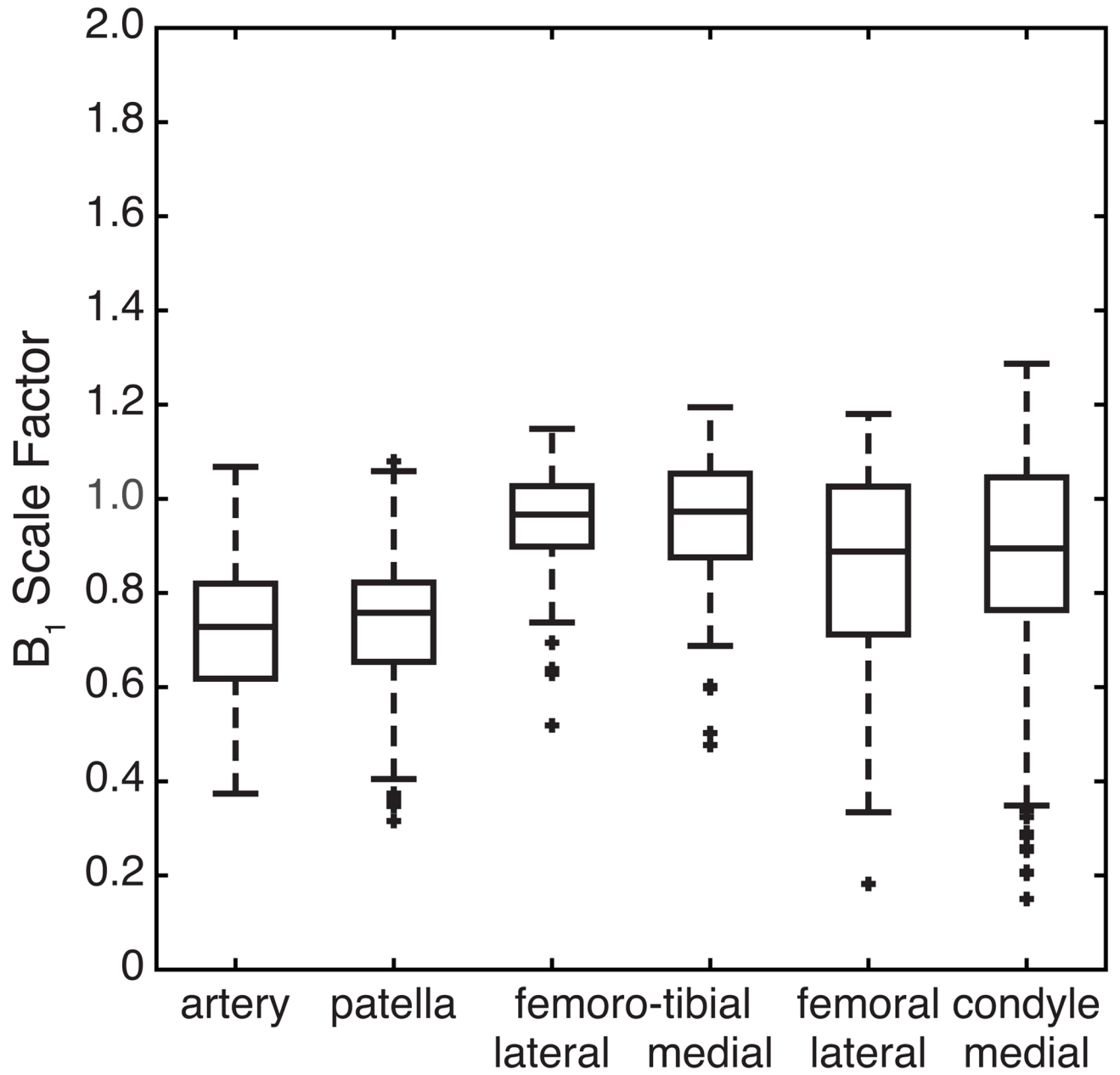
**Figure 5.**
Box plots of the $B_1$ scale factor for individual ROIs on a $^{23}$Na knee image from a healthy volunteer.
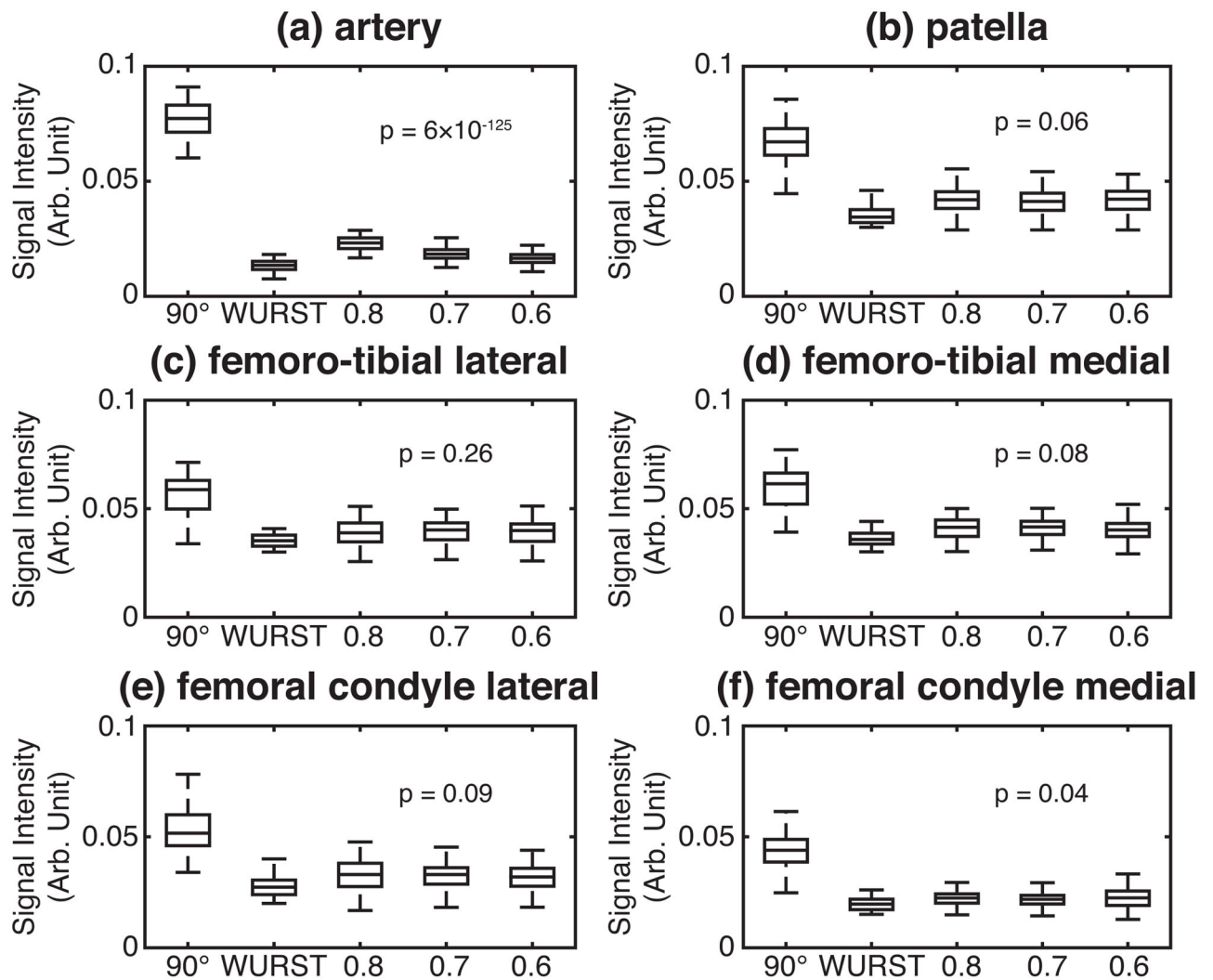
**Figure 6.**

Performances of three OC pulses optimized under different ranges of the RF scale factors. Box plots of the signal intensities are drawn for the individual ROIs: (a) artery, (b) patella cartilage, (c) lateral femoro-tibial cartilage, (d) medial femoro-tibial cartilage, (e) lateral femoral condyle cartilage, and (f) medial femoral condyle cartilage. The indices on the x axes indicate the MRI pulse sequences used: '90°' for $^{23}$Na MRI without fluid suppression; 'WURST' for fluid-suppressed $^{23}$Na MRI performed with the WURST pulse; '0.8', '0.7', and '0.6' for fluid-suppressed $^{23}$Na MRI performed with the OC pulses optimized respectively for the RF scale factors from 0.8 to 1.2, from 0.7 to 1.2, and from 0.6 to 1.2. The p values from one-way ANOVA, performed on the distributions of the signal intensities acquired with the three OC pulses, are displayed.
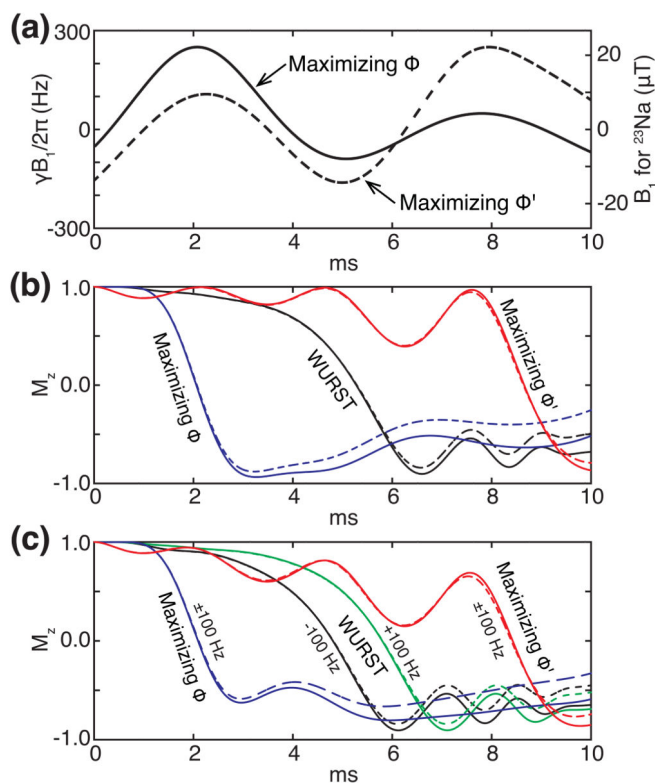
**Figure 7.**
Dependence of OC pulses and their performances on cost functions. (a) The x components of the OC pulses maximizing the cost functions $\varphi$ (solid) and $\varphi'$ (dash). The y components are null. (b) The evolutions of the z components of the magnetization vectors on resonance while applying the WURST pulse (black lines) and the OC pulses maximizing the cost functions $\varphi$ (blue lines) and $\varphi'$ (red lines). (c) The evolutions of the z components of the magnetization vectors at ±100 Hz while applying the WURST pulse (black and green lines) and the OC pulses maximizing the cost functions $\varphi$ (blue lines) and $\varphi'$ (red lines). For the OC pulses, the trajectories for −100 Hz and +100 Hz coincide. The straight and dashed lines respectively represent the systems with the relaxation times 38 ms and 20 ms.

**Table 1**

$B_1$ scale factors estimated in the arteries.

| Subject # | Mean | Standard deviation | Better fluid suppression |
|-----------|--------|--------------------|--------------------------|
| 1 | 0.8325 | 0.1012 | WURST |
| 2 | 0.8181 | 0.0542 | OC |
| 3 | 0.8101 | 0.1552 | WURST |
| 4 | 0.8547 | 0.0891 | OC |
| 5 | 0.8877 | 0.1275 | same |